A Discrete Ordinate, Multiple Scattering, Radiative Transfer Model of the Venus Atmosphere from 0.1 to 260 μm

CHRISTOPHER LEE AND MARK IAN RICHARDSON

Ashima Research, Pasadena, California

(Manuscript received 12 October 2010, in final form 18 January 2011)

ABSTRACT

The authors describe a new radiative transfer model of the Venus atmosphere (RTM) that includes optical properties from nine gases and four cloud modes between 0.1 and 260 μm. A multiple-stream discrete ordinate flux solver is used to calculate solar and atmospheric infrared fluxes with a prescribed temperature profiles and calculate radiative–convective equilibrium temperatures using the model.

Components of the RTM are validated using observations from *Pioneer Venus* and *Venus Express*. A visible bond albedo of 0.74 and subsolar surface visible flux of 50 W m^{-2} [4.0% of the top-of-atmosphere (TOA) insolation] are calculated for a suitable temperature and composition profile derived from the Venus International Reference Atmosphere. Solar fluxes are simulated over a range of latitudes and good agreement is found with results from the *Pioneer Venus* probes and *Venera* landers. TOA infrared fluxes are compared with *Venus Express* observations and found to compare well at all observed wavelengths.

The RTM is used to calculate radiative heating rates and these calculated heating rates are compared with those prescribed in a modern Venus GCM. Modifications are suggested to improve the prescribed thermal forcing used in recent GCMs. Using a small family of numerical and physical configurations, little sensitivity to vertical resolution is found in the model. For suitable global mean solar forcing a surface temperature of 750 K at radiative–convective equilibrium is calculated, in good agreement with observations and other recent modeling efforts.

1. Introduction

The atmosphere of Venus contains over 90 bars of carbon dioxide (Colin 1983) and has a surface temperature of almost 750 K. Trace amounts of water and sulfur dioxide combine to produce a dispersed hazelike cloud composed of aqueous sulfuric acid (e.g., Esposito et al. 1997) that extends from 30 to 70 km over most of the atmosphere.

A number of models have been developed in an attempt to simulate the atmosphere of Venus, with greater success in the past decade. Pollack and Young (1975) developed a relatively simple radiative transfer model (RTM) that included clouds and absorption from carbon dioxide and water and used this model to calculate a radiative–convective temperature that was close to the observed profile and exhibited the familiar ''greenhouse'' warming (Ingersoll 1969). After the *Pioneer Venus* mission, Crisp (1986, 1989) developed a radiation model for the middle and upper atmosphere (above 50 km) that included much of the information that was learned from the *Pioneer Venus* probes (e.g., Seiff et al. 1980) and orbiter (e.g., Taylor et al. 1980). This model included data on carbon dioxide, water, and sulfur dioxide; a Mie scattering cloud model of sulfuric acid clouds; and the capability to simulate IR and solar fluxes above the clouds.

The model developed by Bullock (1997) is similar to the Crisp (1986) model but includes additional absorbers and extends the model from the surface to 100 km, using prescribed solar fluxes (Tomasko et al. 1980) to describe the solar insolation. This model was used to drive an evolutionary model of the Venus atmosphere (Bullock and Grinspoon 2001) that included basic chemistry and geologic evolution to predict the state of the Venus atmosphere in the recent past.

The most recent radiative transfer model applied to Venus, the *K*-distribution Atmospheric Radiation: Infrared Net Exchange model (Eymet et al. 2005), uses a Monte Carlo algorithm to calculate IR exchanges

Corresponding author address: Christopher Lee, Ashima Research, 600 S. Lake Ave., Suite 104, Pasadena, CA 91101.
E-mail: lee@ashimaresearch.com

DOI: 10.1175/2011JAS3703.1

between layers of the atmosphere and between the atmosphere, space, and the ground. The results from this model are then used to construct a net exchange rates (NER) dataset, collating the results from the slow and accurate Monte Carlo model into a form useable within a GCM (Lebonnois et al. 2010). The spectral data used in this model are based on the Bullock (1997) data, with no sub-Lorentzian CO_2 line broadening, and a prescribed solar flux model based on Tomasko et al. (1980).

We have continued the study of the radiative state of the Venus atmosphere using radiative transfer models by developing a flexible model capable of simulating the radiative fluxes over a wide spectral range (currently 0.1–260 μm), including the optical properties of nine absorbing gases, three cloud modes, and the unknown UV absorber (Esposito et al. 1997; Crisp 1986). We include optical properties for the gases derived from a high-resolution tabulation of a line database, Rayleigh scattering and continuum absorption for the most radiatively active gases, and Mie-scattering optical properties for the clouds. We continue to use a two-stream flux solver (TWOSTR) (Kylling et al. 1995) but additionally (and independently from TWOSTR) employ a multiple-stream multiple scattering Discrete Ordinate Radiative Transfer model (DISORT) (Stamnes et al. 2000). Both flux solvers use discrete ordinate methods, with delta-*M* transformation, and limited treatment of spherical atmospheres. Importantly, we calculate radiative fluxes due to atmospheric emission and solar fluxes [Bullock (1997) and Lebonnois et al. (2010) prescribe the solar component] and calculate fluxes over a wider spectral range, and with higher resolution, than other published models (Crisp 1986, 1989; Bullock 1997; Lebonnois et al. 2010).

Using this model we have been able to successfully simulate radiative fluxes below 1 μm at the top and bottom of the atmosphere and near-IR and thermal infrared fluxes within the Visible and Infrared Thermal Imaging Spectrometer (VIRTIS) passband (Drossart et al. 2007) and have calculated fluxes within the atmosphere that are in agreement with the limited number of observations (Seiff et al. 1980). We have also used this model to calculate radiative and radiative–convective equilibrium temperature profiles for a *typical* Venus composition profile (Kliore et al. 1985) and compared the temperature structure, flux profile, and lapse rates to observational data.

The goal of this work is to develop a radiative transfer model that calculates the radiative fluxes over a wide spectral range that includes the solar fluxes and water continuum and far-infrared wavelengths, from which we can produce a much simplified and faster radiative parameterization that can be used within a Venus GCM. As such we have endeavored to produce a consistent and complete RTM that produces realistic spectra throughout the entire atmosphere, given a plausible temperature and composition profile, including explicit solar flux calculations instead of prescribing the profile based on observations and modifying the gaseous absorption properties where necessary for the thick Venus atmosphere. The next stage of our work is to find suitable approximations and simplifications that will increase the speed of the RTM while maintaining sufficient accuracy to provide the radiative forcing in a GCM.

In section 2 we describe the new radiative model in detail, listing the sources of absorption and scattering and describing the method used to calculate optical properties and fluxes. In section 3 we examine the model with two relatively broad validation tests. First, we calculate the radiative properties of the temperature and composition profile described in the Venus International Reference Atmosphere (VIRA) (Kliore et al. 1985) and then calculate outgoing radiances between 1 and 4 μm to compare with sample nighttime observations from the *Venus Express*/VIRTIS instrument (Drossart et al. 2007).

In section 4 we conduct two experiments of interest to the radiative forcing of a Venus GCM. First, we use the RTM to analyze the fluxes and heating rates from a prescribed temperature profile in a GCM (Lee et al. 2007) and compare the RTM simulated heating rates to the prescribed heating rate used in the GCM. Second, we calculate the radiative and radiative–convective equilibrium temperature profiles using the RTM and compare these simulated equilibrium temperature profiles to those derived from observations (Kliore et al. 1985) and then calculate the vertical temperature lapse rate for each profile to identify the convectively unstable layers in the atmosphere.

2. The radiative transfer model

The RTM that we have developed has two independent components. The first component calculates the optical properties of the atmosphere for a prescribed temperature and composition profile, and the second component calculates radiative fluxes based on the temperature and optical properties of the atmospheric profile.

Optical properties are calculated for nine gases and three cloud modes. The gases are carbon dioxide (CO_2), water (H_2O), nitrogen (N_2), carbon monoxide (CO), sulfur dioxide (SO_2), carbonyl sulfide (OCS), hydrogen sulfide (H_2S), hydrogen fluoride (HF), and hydrogen chloride (HCl). We use parameters from the 2004 High-Resolution Transmission Molecular Absorption (HITRAN) database (Rothman et al. 2005) and the High-Temperature Spectroscopic Absorption Parameters (HITEMP) CO_2 database (Rothman et al. 1995) to specify

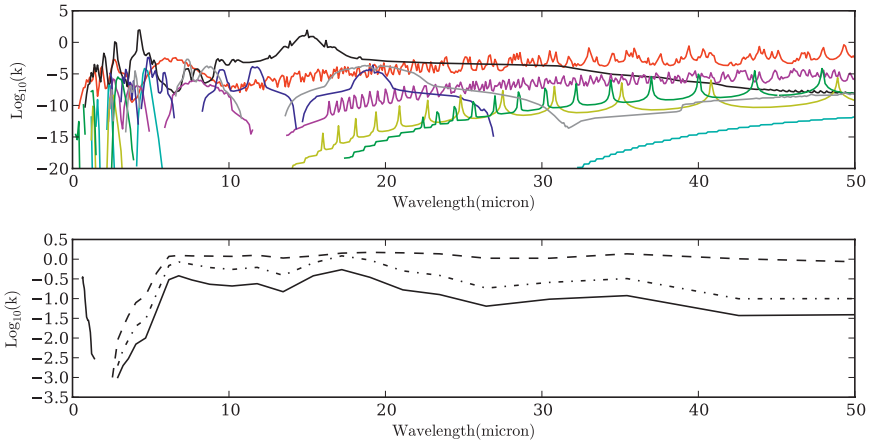

FIG. 1. (top) Absorption coefficients calculated at approximately 100 kPa and 300 K, scaled by an approximate VMR for Venus. Line data from HITRAN 2004 (Rothman et al. 2005) and HITEMP (Rothman et al. 1995), tabulated using methods outlined in Lacis and Oinas (1989). (bottom) Cloud mode 1 + UV absorber (solid) and cloud modes 2 (dotted) and 3 (dashed).

the line parameters for each gas. For most of the gases considered, the HITRAN line data extends from 0.25 to at least 260 μm, and HITEMP CO_2 data extend from 0.78 to 25 μm. We include all spectral lines in both databases, assuming a terrestrial isotope distribution for all gases except hydrogen, and a number of pseudocontinua in the UV–visible region, as discussed below.

We calculate and store tabulated optical data using the correlated-*k* method, outlined in Lacis and Oinas (1989), using a model developed by Irwin et al. (1997, 2008). For each species we precalculate the absorption coefficient at 20 reference temperatures, separated by 50 K between 150 and 1100 K, and 20 reference pressures, distributed logarithmically in pressure space between 0.1 Pa and 14 MPa, and at a fixed spectral resolution depending on the application. When calculating the spectrally dependent opacity for each molecule, we truncate the calculation of each line at 350 cm^{-1} from the line center. This truncation speeds up the calculation significantly, but we require continuum models (discussed below) to account for absorption in the very far wings of each line. In this study we use *K*-tables with spectral resolutions at 0.0005 μm when comparing with *Venus Express* VIRTIS data, and a variable-resolution *K*-table when calculating visible albedos, net fluxes, and heating rates. The variable-resolution bins are 0.02 μm wide from 0.09 to 2.55 μm, 0.1 μm wide from 2.55 to 22.75 μm, 1.0 μm wide from 22.75 to 40.75 μm, 10.0 μm wide from 40.75 to 100.75 μm, and 40 μm wide from 100.75 to 260.75 μm. The boundaries are chosen to fill the spectral space completely and uniquely, and are chosen to balance the calculation cost against accuracy gain from using the highest resolution available. In each case, the spectral data are stored using 20 Gaussian points (Weisstein 2003) to allow numerical quadrature in each wavelength bin within the RTM. This tabulated data is used within the RTM by interpolating from the precalculated values to the required temperature and pressure.

Figure 1 shows the absorption coefficients of the line-absorbing gases (i.e., excluding N_2) between 0.1 and 50 μm, calculated at approximately 100 kPa and 300 K, scaled by an appropriate concentration for the Venus atmosphere (Kliore et al. 1985). The important features in this plot are absorption by carbon dioxide in three large bands at 2.7, 4.3, and 15 μm and absorption by water at longer wavelengths (>25 μm) and within the 8-μm region where CO_2 absorption is small. These five spectral regions contribute to a radiative warming (the greenhouse effect) in the Venus atmosphere. Sulfur dioxide has large magnitude, narrow absorption features near 8 μm; carbonyl sulfide contributes to the opacity at about 6 and 12 μm. In the absence of water, hydrogen sulfide would dominate above 25 μm.

We assume self-broadening when calculating the CO_2 opacities [with a volume mixing ratio (VMR) of 96.5%] and air-broadening when calculating the opacities of all other gases. We modify the line shape of the carbon dioxide absorption following Meadows and Crisp (1996) to provide a sub-Lorentzian line shape. This modification is required when fitting the high-resolution spectra available in the near-IR windows and affects the heating rates in the lower atmosphere. We include modifications to the line and continuum absorption by water following Clough et al. (1989).

In addition to the calculation of the *K*-table for each gas, we include collision-induced continuum absorption for CO_2 (Moskalenko et al. 1979) and continuum absorption for H_2O (Clough et al. 1989). We include

parameterized ultraviolet absorption for SO_2 (Manatt and Lane 1993), H_2S (Feng et al. 1999), HCl (Brion et al. 2005), N_2 (Chan et al. 1993), and OCS (Molina et al. 1981). We include Rayleigh scattering for CO_2, H_2O, and N_2 (Washburn and West 1926; Goody and Yung 1995).

We use a cloud model based on a Mie scattering parameterization. Cloud modes 1–3 (Esposito et al. 1997) are included in the model using the scattering and extinction efficiencies given in Crisp (1986, 1989). Optical parameters given in that work assume a cloud composition of 75% sulfuric acid and 25% water, using refractive index data from Palmer and Williams (1975). We additionally include the empirical UV absorber modification to the mode-1 optical parameters and composition profile described in Crisp (1986). Data from Palmer and Williams (1975) extend from 0.36 to 25 μm; outside of this region we follow Crisp (1986) by using the optical parameters at 0.36 μm below this wavelength and the optical parameters at 25 μm above this wavelength.

We calculate the extinction and scattering coefficients of each atmospheric layer by first calculating the appropriate coefficients for each gas and cloud type and then combining these coefficient values using the method outlined in Lacis and Oinas (1989). A Henyey–Greenstein model is used for the particulate Mie scattering, which requires a scattering asymmetry parameter g for each scattering layer, which we calculate as a weighted mean of the individual asymmetry parameters within each layer, using the total layer scattering optical depth as the weight in the calculation (Bullock 1997); that is,

$$\overline{g} = \frac{\sum_i s_i g_i}{\sum_i s_i}, \tag{1}$$

where s_i is the scattering coefficient and g_i is the asymmetry parameter of the ith constituent.

To calculate the fluxes in the atmosphere using the RTM, we use the DISORT (Stamnes et al. 2000) or TWOSTR (Kylling et al. 1995) flux solvers (independently selectable during the calculation). DISORT requires absorption and scattering coefficients, scattering phase functions, and single-scattering albedo. TWOSTR requires similar parameters, substituting an asymmetry parameter for the scattering phase function (Goody and Yung 1995). These parameters are calculated for each profile and wavelength range prior to invoking the flux solver. Both flux solvers are used unmodified except to allow compilation and interface with the opacity calculation. The vertical grid of each flux solver is set to the vertical grid used to define the optical properties of the atmosphere in each experiment (either 81 or 32 in this manuscript), and the surface skin temperature in the model is set to be the temperature of the lowest defined layer. In the DISORT flux solver, we use eight streams, with an angular resolution of 45° in azimuth and polar angles.

The top-of-atmosphere (TOA) solar downward flux is specified using a blackbody function with a solar temperature of 5850 K and orbital radius of 0.72 AU (Colin 1983), to give an integrated TOA insolation of $\sim$2670 W m^{-2}. We first calculate the solar fluxes with no atmospheric emission (referred to in this manuscript as a *solar* calculation) and then calculate the atmospheric fluxes with no TOA solar insolation (referred to as an *IR* calculation). Both solar and IR calculations are made over the same wavelength range and fluxes are returned as upward, downward diffuse, and downward direct (i.e., solar beam) fluxes. Where global mean fluxes are required we calculate solar fluxes at 5° latitude intervals and use this data to derive a global mean flux. The bulk of the flux solver calculation may be carried out in parallel using a distributed memory interface [Message Passing Interface (MPI)] (Gropp et al. 1999).

The RTM we have developed is likely too slow to use directly within a GCM. A single DISORT flux calculation, using 343 spectral bands for a solar and atmosphere calculation, takes approximately 2 h on a single processor. A single TWOSTR flux calculation under the same conditions takes approximately 5 s. Both flux solvers are too slow, especially when considered for a GCM with thousands of grid points requiring the same calculation for different temperature and composition profiles. The preferred approach is still being investigated but the likely compromise between accuracy and speed will be to parameterize the results of the slow, yet accurate, calculation for use in the GCM (Lebonnois et al. 2010). It is possible that the TWOSTR flux solver may be usable directly within the GCM, but this would require a factor of 1000 decrease in run time—possible only by reducing the spatial and spectral resolution of the model.

3. Validation

We now present our current validation efforts using this RTM. We begin by using the VIRA (Kliore et al. 1985) to specify the atmospheric temperature and composition profiles. Using these profiles we calculate atmospheric fluxes, albedo, weighting functions, and heating rates. Our goal is not to replicate a particular observation, and especially not to retrieve the atmospheric state during these observations, but rather to verify that the RTM is able to reproduce the features that are observed in spectra of the Venus atmosphere. The RTM has no

retrieval model (Rodgers 2000) and cannot ingest observational data; as such, we do not attempt to "fit" the observations with our model. Our second test of the RTM is to calculate the IR fluxes between 1 and 4 μm at the resolution of the VIRTIS-M instrument on *Venus Express* (Drossart et al. 2007), which is then compared with a sample observation from VIRTIS-M.

a. Venus International Reference Atmosphere

The VIRA (Kliore et al. 1985) model includes temperature profiles for five latitudes (0°–30°, 45°, 60°, 75°, and 85°) above 35-km altitude and a single profile between the surface and 35 km. The model additionally includes compositional information for the nine gases used in the RTM between at least 0 and 100 km. Figure 2 shows the temperature profile for each of the five latitudes and the composition profile (Tomasko et al. 1980; Kliore et al. 1985; Bullock 1997) used in this study.

The VIRA temperature profile is essentially an adiabatic (or near adiabatic) lower atmosphere between 0 and 60-km altitude, capped by a stratosphere up to at least 100 km. The variation in temperature with latitude seen in the VIRA model (at 60–80 km) is related to radiative and dynamical processes in the atmosphere, such as the overturning circulation (Lee et al. 2007) and the warm-pole feature (Taylor et al. 1980). The composition of the VIRA atmosphere is approximately 96.5% carbon dioxide, 3.5% nitrogen, <0.1% water, 1–100 ppmv sulfur dioxide, 1–100 ppmv carbon monoxide, 1–10 ppmv carbonyl sulfide, 1 ppmv hydrogen chloride, and 1 ppbv hydrogen fluoride.

The cloud properties used in this study are derived from observations by the *Pioneer Venus* Cloud Particle Size Spectrometer (LCPS) Experiment (Knollenberg and Hunten 1980). The LCPS observations were used to define the three modes used by Crisp (1986) that are used in our model. The cloud number densities from Knollenberg and Hunten (1980) have been interpolated onto our VIRA pressure grid using the altitudes given by the VIRA dataset. Figure 3 shows the vertical profiles of the three cloud modes used in this study, essentially smoothed versions of the high-resolution data given in Fig. 16 of Knollenberg and Hunten (1980).

Using this temperature and composition profile we calculate the global-mean fluxes within the atmosphere and from this derive the mean solar and IR heating rates. In Fig. 4 we show the fluxes throughout the atmospheric column and also the corresponding flux convergence and heating rates, for each of the solar and IR components, and the combined fluxes. In calculating the heating rates we assume that heat capacity varies with

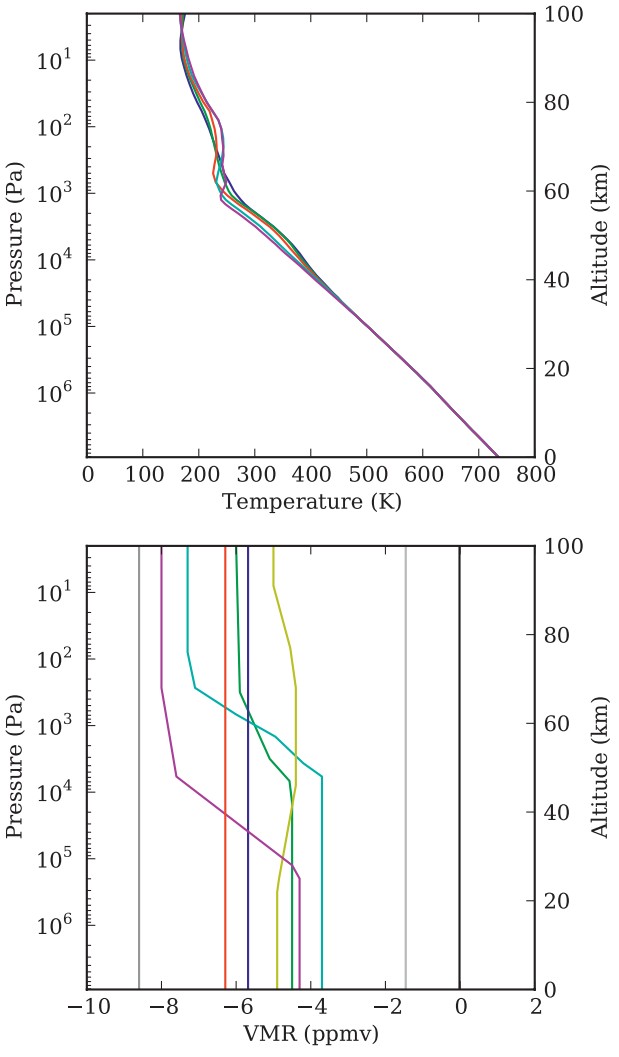

FIG. 2. (top) Temperature profiles given in VIRA (Kliore et al. 1985) at 0°–30° (black), 45° (red), 60° (green), 75° (blue), and 85° (magenta) latitude. (bottom) VIRA composition used in this study is CO_2 (black), H_2O (red), HCl (blue), OCS (green), CO (magenta), H_2S (cyan), HF (yellow), SO_2 (light gray), and N_2 (dark gray).

temperature but not pressure, as defined in Crisp (1986), and that gravity varies as

$$g = g_* \frac{1}{(1 + z/R)^2}, \tag{2}$$

where g_* is the gravitational acceleration at the surface (8.87 m s^{-2}), R is the planetary radius (6041 km, assumed to be a sphere), and z is the layer altitude.

The lower atmosphere in this calculation is dominated by the IR fluxes that can exceed 15 kW m^{-2} at the surface. However, the upward and downward fluxes almost cancel in the *net* and produce very little heating.

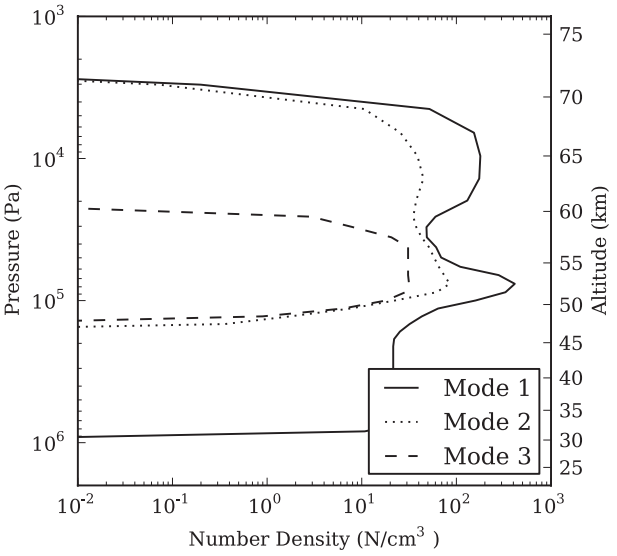

FIG. 3. Cloud composition used in this study, from Knollenberg and Hunten (1980), for cloud mode 1 + UV absorber (solid) and cloud modes 2 (dotted) and 3 (dashed line).

Only at the model top, above 100 Pa, does the cooling exceed 10 K per Earth day [resulting in the observed day − night temperature difference; Seiff et al. 1980].

The solar fluxes dominate in the upper atmosphere with most of the absorption of the solar fluxes occurring within the cloud decks between 100 kPa and 1 kPa. Above the clouds, there is little absorption by either gas or clouds in the atmosphere, and the net fluxes are relatively constant. Below the clouds there is very little net downward solar flux (a few percent reaches the surface, as we show in the next section). The absorption within the cloud deck, up to 10 W m^{-2} km^{-1}, results in heating of the atmosphere at the cloud tops.

The combined solar and IR net heating in this profile tends to cool the atmosphere within the clouds, while heating occurs at the bottom of the cloud decks and at the top of the atmosphere. Very little heating occurs in the lower atmosphere. At the subsolar point (not shown), there is significantly more solar absorption in the cloud decks, up to 60 W m^{-2} km^{-1}, causing a 20 K per Earth day heating rate at 10 kPa. The noontime upper atmosphere has an extreme (but short lived) heating rate of more than 100 K per Earth day. The extreme heating and cooling rates above 10 Pa are reflected in the *Pioneer Venus* probe (Seiff 1983) observations of the upper atmosphere temperature, where a temperature difference of more than 200 K was observed between the *Day* and *Night* probes.

For the same VIRA reference profile, Fig. 5 shows the albedo below 1 μm. The shape of the spectrally dependent albedo is in reasonable agreement with observations (Titov et al. 2007; Moroz 1983) with a relatively

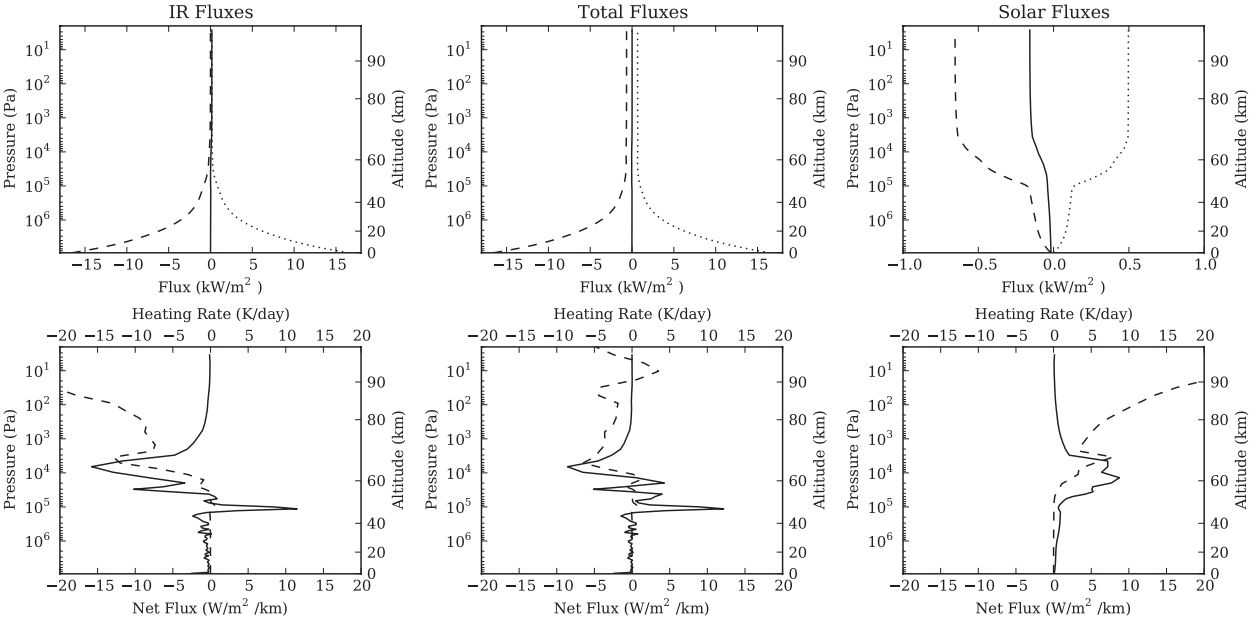

FIG. 4. Globally averaged fluxes and heating rates calculated for the temperature and composition profile given in Figs. 2 and 3. IR fluxes refer to atmosphere-only fluxes; solar fluxes refer to radiation from the simulated sun. Both IR and solar fluxes are calculated from 0.1 to 260 μm. (top) Upward (dotted), downward (dashed), and net (solid) fluxes in the (left) IR, (right) solar, and (middle) total fluxes. (bottom) Net flux (solid) and instantaneous heating rate (dashed–dotted) for the (left) IR, (right) solar, and (middle) total fluxes. All fluxes are shown as upward positive. Heating rates are positive for warming.

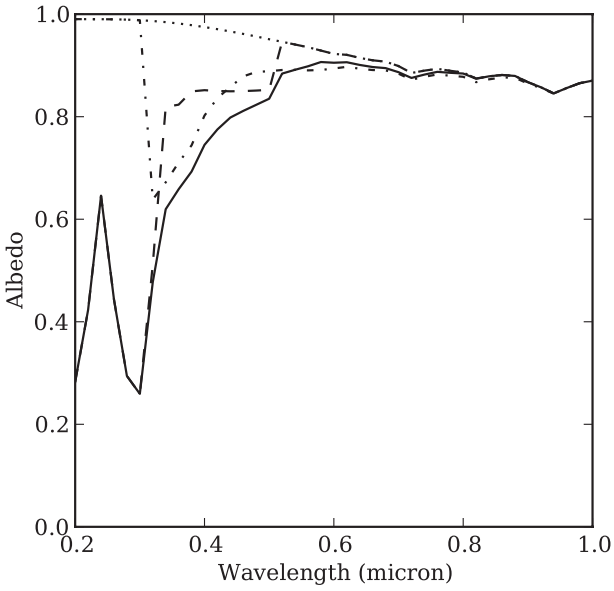

FIG. 5. Albedo calculated at the subsolar point: nominal case (solid), no sulfur dioxide UV absorption (dashed), no unknown UV absorber (dotted), and no sulfur dioxide and no UV absorber (dashed–dotted).

broad visible spectrum of reflected sunlight, with a minimum albedo of 0.25 at 0.3 μm. The geometric albedo at 550 nm is 0.89 and the bond albedo (Moroz 1983) is 0.82. Integrated over the 0.35–0.75-μm (350–750 nm) region, the geometric and bond albedos drop to 0.84 and 0.74, respectively. Observations of the albedo vary somewhat but are generally close to these values. Taylor et al. (1980) reported a value of $0.76^{+0.02}_{-0.03}$ for the integrated bond albedo; Moroz (1983) reported 0.75 ± 0.03 for the integrated bond albedo and 0.85 ± 0.03 for the geometric albedo; Moroz et al. (1985) reported 0.76 ± 0.01 and Tomasko et al. (1980) reported 0.8 ± 0.02 for the bond albedo. The albedo values produced by our model are within the errors of some of the observations and are in agreement with all observations considering the variation observed in the atmospheric opacity (Moroz 1983).

Excluding the gaseous UV absorption [predominantly by a sulfur dioxide continuum; Manatt and Lane 1993] changes the absolute albedo values by less than 4%, increasing the integrated albedo and decreasing the 550-nm albedo (dashed line in Fig. 5). Excluding the unknown UV absorber [as parameterized by Crisp (1986)] increases the albedos by up to 8% (dotted line in Fig. 5). Excluding both UV absorbers increases the albedo by up to 15%. Table 1 summarizes these results.

Figure 6 shows the downward solar flux at the surface for the same calculations as above. At the subsolar surface, approximately 4.0% (49.2 W m^{-2} between 350 and 750 nm) of the incoming insolation reaches the surface in the nominal case. All of the insolation reaches the surface in the diffuse component of the solar flux, not the direct beam, suggesting that the sun is undetectable as a light source on the surface. Almost no IR (i.e., atmospheric) flux is present (0.02 W m^{-2}) below 1 μm at the surface, suggesting that the lower atmosphere is dark during the Venus night (at least at midnight, when very little solar radiation will reach the surface through scattering). When the sulfur dioxide absorption is omitted, a further 11.9 W m^{-2} reaches the surface mainly through increased UV light. When the UV absorber is omitted, 2.1 W m^{-2} additional flux reaches the surface, mainly in blue light.

Figure 7 shows the integrated full-spectrum (0.1–260 μm) downward solar flux at the surface as a function of solar zenith angle. The results from our model agree very well with the results shown in Tomasko et al. (1980) and with the six lander or probe measurements shown in the figure. Results from both the DISORT flux solver and TWOSTR flux solver are shown in the figure, and both are in good agreement over all angles, diverging most significantly at the subsolar point (where they differ by about 5%).

For the same VIRA temperature and composition profile, we calculated the weighting functions in the so-called ''window'' regions (Allen and Crawford 1984) of 1.0, 1.7, and 2.3 μm (Tsang et al. 2008a), using *K*-tables

TABLE 1. Simulated albedos calculated using wavelengths between 350 and 750 nm (rows 1 and 2) and calculated to 550 nm (rows 3 and 4); bond albedo calculated as in Moroz (1983) (rows 5 and 6). Surface fluxes are given in W m^{-2} and percentage of TOA solar flux between 350 and 750 nm.

	Nominal	No sulfur UV absorber	No ''unknown'' UV absorption	No UV or sulfur absorption
		Simulated albedo		
Integrated bond albedo	73.7	76.9	80.9	88.9
Integrated geometric albedo	84.3	86.3	88.9	93.7
550-nm bond albedo	81.8	81.2	89.0	93.8
550-nm geometric albedo	89.2	89.1	93.8	93.8
		Surface fluxes between		
350 and 750 nm (W m^{-2})	49.2	61.1	51.3	66.9
350 and 750 nm (%)	4.0	5.0	4.2	5.4

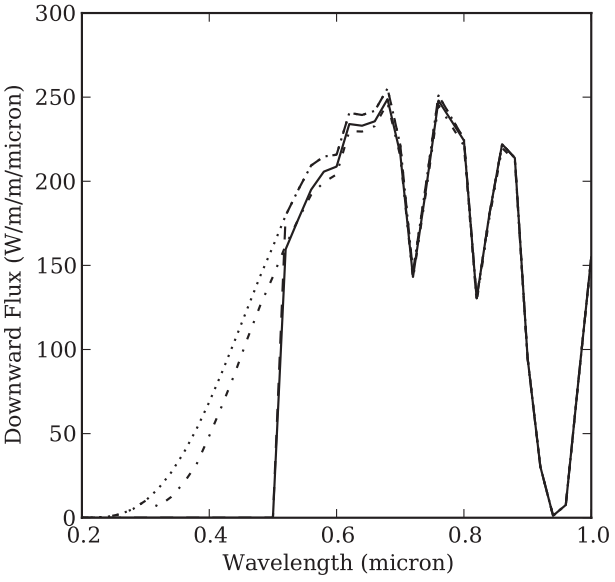

FIG. 6. Downward solar flux at the surface at the subsolar point: nominal case (solid), no sulfur dioxide UV absorption (dashed), no unknown UV absorber (dotted), and no sulfur dioxide and no UV absorber (dashed–dotted).

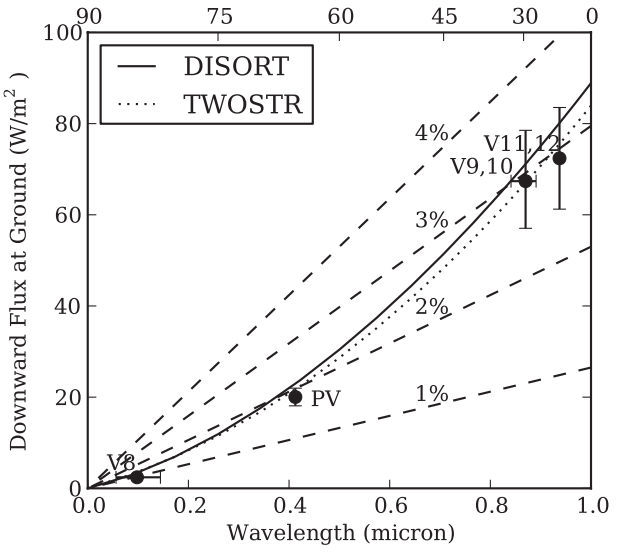

FIG. 7. Downward solar flux at the surface calculated as a function of solar zenith angle using DISORT (solid) and TWOSTR (dotted). Also plotted as dashed lines are lines representing 1%–4% of the TOA flux as a function of latitude, and lander observations from Tomasko et al. (1980) for *Pioneer Venus* and *Venera 8*, *9*, *10*, *11*, and *12*.

with a resolution of 0.0005 μm [approximately half the VIRTIS-M resolution, Drossart et al. (2007)]. Weighting functions J are calculated by explicitly perturbing each layer in turn by 1 K and recalculating the TOA outgoing fluxes, using

$$J(\lambda, z) = \frac{\partial F^{\mathrm{TOA}}(\lambda)}{\partial T(z)}, \tag{3}$$

where $T(z)$ is the temperature at altitude z and $F^{\mathrm{TOA}}(\lambda)$ is the top-of-atmosphere outgoing flux at wavelength λ. These weighting functions are shown in Fig. 8 after normalization, so that the altitude integral equals unity.

As in Tsang et al. (2008a), the 1.01-μm, 1.1-μm, and 1.18-μm windows are most sensitive to fluxes from the surface or near surface, while the 1.27-μm window is sensitive to radiation from the lower 20 km centered near 10 km, and the 1.31-μm window is sensitive to atmospheric temperature between 15 and 30 km. The 1.7-μm band exhibits a peak sensitivity to radiation from 5 to 25 km in the atmosphere (all ''subwindows'' in this region are sensitive to approximately the same region), and the 2.3-μm window exhibits sensitivity to radiation from both the lower atmosphere (at 2.3 and 2.4 μm) and the middle atmosphere (2.5 μm).

b. Venus Express/VIRTIS observation

The next test of our model is to compare the TOA fluxes produced from the RTM with sample output from the *Venus Express* VIRTIS-M instrument (Drossart et al. 2007). Again, our goal is not to reproduce the observed spectra nor retrieve the state vector that produces the observations, but rather to ensure that our model will produce the same spectral features as those observed, given a reasonable temperature and composition profile. All VIRTIS data shown here were retrieved from the NASA Planetary Data System (PDS) dataset in August 2009.

Figure 9 shows the outgoing flux observed by the VIRTIS instrument for a small nighttime region with near-nadir emission from observations VIR0098_17 and VIR0073_05. The important emission features in this figure, and in many similar nighttime and near-terminator emissions, are the 1.0–1.5-μm emissions from the near-surface atmosphere, the 1.7-μm emissions from the low atmosphere, and the 2.0–2.5-μm middle atmosphere sensitive to cloud opacity. The emission above 3 μm is dominated by radiation from above the cloud decks with a blackbody temperature of about 235–250 K. The radiation below 1.5 μm has significant contributions from the scattered sunlight, particularly in the VIR0073_05 observation, which is closer to the terminator.

Using the VIRA temperature profile the calculated outgoing atmospheric radiation is shown in Fig. 10 as a dashed gray line. All of the observed features are present in the RTM, though there is disagreement in the magnitudes of the features. The differences between the observed and modeled spectra are indicative of

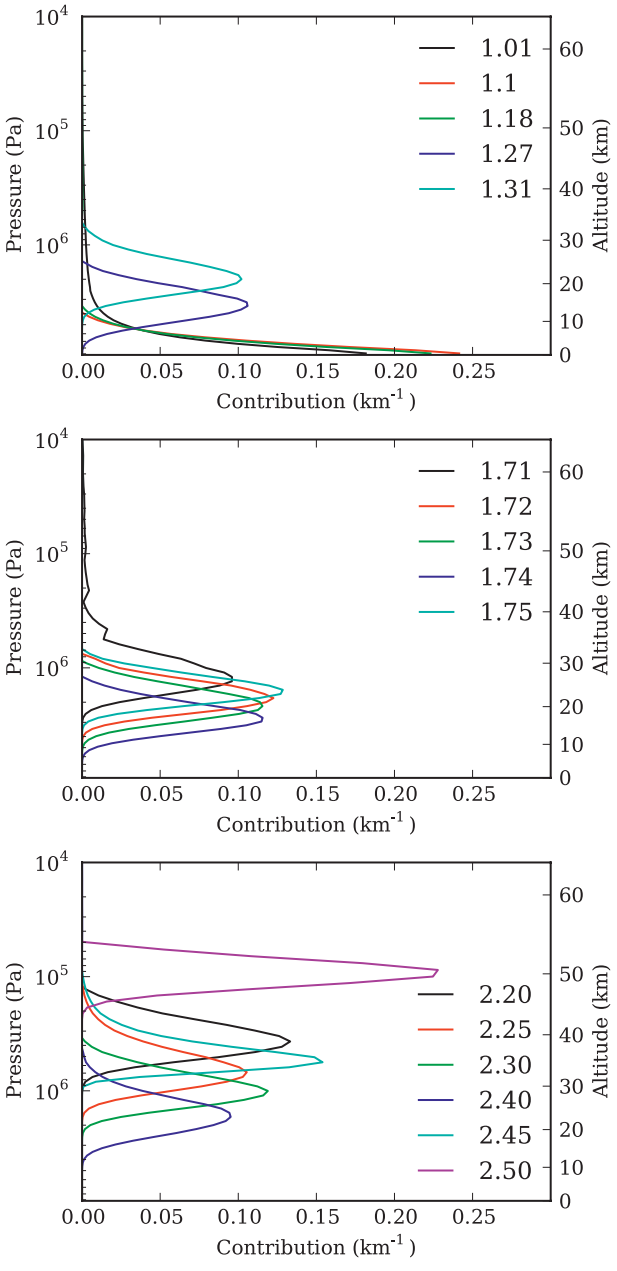

FIG. 8. Normalized contribution functions in the (top) 1-μm, (middle) 1.7-μm, and (bottom) 2.3-μm bands, calculated by explicit perturbation of the temperature profile without scattering but with all absorbers. Units are normalized such that the area integral of each weighting function is unity.

differences in the temperature and composition profile. The solid gray line in Fig. 10 shows the results from increasing the surface and lower atmosphere temperature by 10 K (increasing the 1–1.7-μm fluxes) and increasing the cloud-top temperature by 20 K (increasing the 3–4-μm fluxes). Although the 2–2.5-μm fluxes do change as a result of this perturbation, the overall structure of this

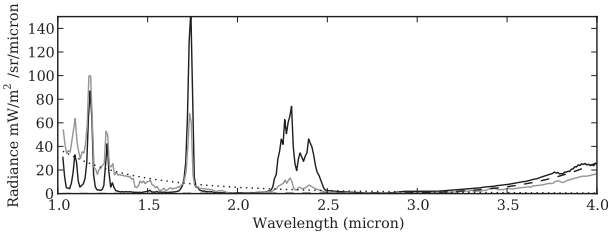

FIG. 9. Sample VIRTIS nighttime observations from the PDS dataset: VIR0098 spectrum (solid black), VIR0073 spectrum (solid gray), scaled TOA solar flux (dashed gray), and blackbody (235 K) radiance (dashed–dotted gray).

feature is more sensitive to composition changes than temperature changes (Tsang et al. 2008a).

It is possible that modifying the composition profile would negate the need to perturb the temperature as we have done, but this type of fitting of the data is better performed using robust statistical estimation methods (Rodgers 2000) that we have not implemented in the RTM.

c. *Discussion*

We have attempted to show that the radiative transfer model that we have developed is capable of simulating correctly the fluxes throughout and exiting the atmosphere using a typical Venus temperature and composition profile. We tested the UV–visible region (sub 1 μm) of the RTM by comparing the calculated albedo and downward surface fluxes with previously reported observations made by satellite (Taylor et al. 1980; Moroz 1983; Moroz et al. 1985) and descent probe measurements (Seiff 1983; Tomasko et al. 1980). The RTM results compare well with the albedo and downward surface flux measurements, predicting values that are within the small family of observations allowing for variation in the temperature and composition profile that we chose (Kliore et al. 1985).

As a comparison with VIRTIS observations (Drossart et al. 2007), and a high-resolution retrieval model used on VIRTIS data (Tsang et al. 2008b), we calculated the weighting functions for the atmospheric windows used to probe the lower atmosphere of Venus and simulated the TOA flux from an observation with a simple viewing geometry and low solar fluxes. The weighting function calculation suggested that the model exhibits the same sensitivity to temperature changes as the Tsang et al. (2008b) model, and the simulated TOA fluxes from our model are a reasonable simulation of the TOA fluxes from the Venus atmosphere.

Finally, as a test of our RTM with broadband solar and IR fluxes we calculated representative mean global flux convergences and heating rates. The simulated fluxes

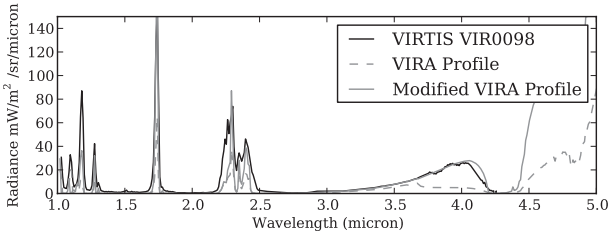

FIG. 10. Simulated VIRTIS nighttime observation using the VIRA composition: VIR0098 spectrum, as in Fig. 9 (solid black); simulated spectrum using the unmodified VIRA temperature profile (dashed gray); simulated spectrum after changing the temperature profile as described in the text (solid gray).

and heating rates agree fairly well with those produced by observations (e.g., Tomasko et al. 1980) and other broadband models (Crisp 1986, 1989; Bullock 1997; Bullock and Grinspoon 2001). In the upper atmosphere, the large daytime solar heating is balanced by IR cooling in the carbon dioxide 15-μm band. The clouds reflect almost 80% of the insolation back to space while absorbing more than 70% of the remaining solar flux. Heating occurs at the bottom of the cloud decks from upwelling IR radiation, with warming inside the clouds from solar radiation. Very little (2%–5%) of the TOA solar insolation reaches the surface to be absorbed there.

4. Experiments

In this section we describe two experiments conducted with the RTM. In the first experiment we apply the RTM to the temperature profile used in the Lee et al. (2007) GCM and compare the heating rates from the RTM with the *prescribed* heating rates in that GCM. Based on this comparison we highlight some errors in the prescribed profile and suggest modifications to the parameterizations used in linearized cooling scheme in Venus GCMs.

In the second experiment, we use the RTM to derive radiative equilibrium and radiative–convective equilibrium temperature profiles. We derive these profiles with two solar flux models: the first calculated internally within the RTM (a "self-consistent" model) and the second using net solar fluxes prescribed from Tomasko et al. (1980).

a. Lee et al. (2007) temperature profile

Lee et al. (2007) described a general circulation model developed using the Hadley Centre Unified Model (Johns et al. 1997). This Venus GCM used a linearized cooling scheme to simulate the radiative heating of the atmosphere. To drive this scheme a temperature profile and heating rates were derived from observed temperature profiles (Seiff et al. 1980) and heating rates (Crisp 1986, 1989), but also empirical models of atmospheric opacity and heating rates. The "relaxed" (radiative equilibrium) temperature field used in the GCM is given in Fig. 11.

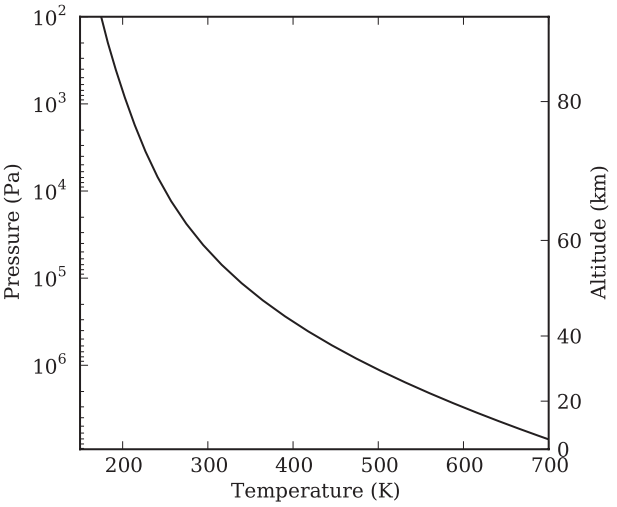

FIG. 11. Prescribed temperature profile used in the Lee et al. (2007) GCM and used here in the RTM to calculate fluxes and heating rates using the polynomial approximation given in Lee et al.

Using our RTM we can calculate the radiative fluxes and resultant heating rates for this temperature profile, which can then be compared to the Lee et al. profile or the similar Yamamoto and Takahashi (2003) profile. To perform the flux calculation with the RTM we assume the VIRA composition profile described above is suitable, as the composition is undefined in the Lee et al. parameterization.

Figure 12 shows the RTM calculated fluxes and heating rates. Although this figure is somewhat similar to the net heating rate and flux convergence shown in Fig. 4, the fluxes here are calculated for a nadir subsolar profile with longitudinally averaged solar heating, as is applied to the GCM. As in the VIRA profile flux calculation (section 3a), almost no flux absorption occurs in the upper atmosphere and very little radiation reaches the lower atmosphere because of the opaque clouds. Most of the absorption of solar radiation occurs at about 60 km within the cloud decks, and IR flux convergence is significant just below at 45–50 km. As a result, most of the radiative heating in the atmosphere occurs just below and above the cloud decks with almost no heating in the lower atmosphere. Significant cooling occurs within the cloud decks because of IR emission. There is a large amount of heating in the upper atmosphere because the atmosphere is thin enough that very little flux absorption is required to cause significant heating.

Figure 12 also shows the equatorial heating prescribed in the GCM. Although the GCM heating occurs in approximately the correct pressure range (i.e., within the

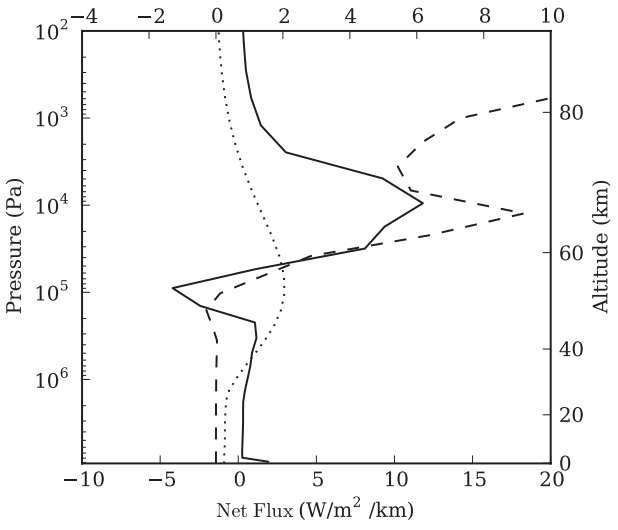

FIG. 12. Net flux convergence (W m^{-2} km^{-1}) (solid, bottom scale) and heating rate (K day^{-1}) (dashed, top scale) for the temperature profile given in Fig. 11, calculated using the RTM. The net flux convergence is calculated as the difference between incoming and outgoing fluxes into each layer, normalized by the thickness of the layer. Heating rate prescribed in the Lee et al. (2007) GCM, as applied to global mean temperature profile (dotted).

cloud region), there are significant differences between the altitude dependence of the heating calculated by the RTM and that prescribed in the GCM.

One difference that has been noted by other authors (Yamamoto and Takahashi 2006; Hollingsworth et al. 2007), which our RTM calculation confirms, is that the prescribed heating rate in the lower atmosphere is far higher than the observed heating calculated from descent probe flux measurements (Seiff et al. 1980). The small constant heating in the lower atmosphere of the GCM is applied partly to simulate a convective stabilization that is expected to occur there (the temperature profile is adiabatic in the lower atmosphere). However, the RTM does not account for this fact and, when considered as a *radiative* heating alone, the prescribed heating is too large.

The GCM heating captures some of the heating in the middle atmosphere but is too broad and small (2 K day^{-1} peak) according the RTM calculation (6 K day^{-1} peak). The prescribed heating is too simple to capture the variation in the heating due to the cloud decks. The heating in the RTM can be separated into two main regions: solar heating at the cloud top (60 km) and IR heating at the cloud base (40 km) with a small amount of IR cooling in between these layers. The IR cooling is missing from prescribed heating because a simple Gaussian-like heating function was chosen to represent the net heating profile.

DISCUSSION

Based on this brief analysis, we propose two changes to the prescribed radiative forcing given in Lee et al. (2007). First, the lower atmosphere convective heating should be parameterized separately from the radiative forcing to differentiate the contribution from radiative forcing and convective adjustment in the lower atmosphere. Second, the radiative heating profile should include the IR cooling within the clouds to simulate the cloud-level heating and IR feedback more realistically.

b. Radiative–convective equilibrium calculation

The reference temperature and composition profile shown in Figs. 2 and 3 is not in radiative equilibrium. A radiatively equilibrated profile would have no net flux convergence and no net heating. The net heating calculated for the VIRA profile (Fig. 4) suggests that the radiative equilibrium state will be warmer than this temperature profile, the additional thermal energy being distributed as necessary to produce a temperature profile with no net heating.

In this section we use the radiative transfer model to calculate the radiative equilibrium temperature (RET) profile for the VIRA *composition* described above. This calculation is both a good test of the ability of the RTM to maintain a stable greenhouse (Ingersoll 1969) atmosphere, and also a necessary starting point for more useful GCM parameterizations such as newer linearized heating and convection parameterizations or Curtis matrix implementations (Goody and Yung 1995). For example, the linearized cooling model used by Lee et al. (2007) relies on the results from single-column models such as Pollack and Young (1975) to derive suitable heating rates for a GCM, and Yamamoto and Takahashi (2003) used the relaxed temperature state and time scales derived by Pollack and Young (1975) in their GCM.

To calculate the radiative equilibrium temperature we follow a procedure similar to that described in Bullock (1997) (see also Bullock and Grinspoon 2001). For a given temperature (and fixed composition) profile, we calculate a Jacobian J that describes the sensitivity of the net upward fluxes F to changes in the temperature profile T:

$$J_{kl} = \frac{\partial F_k}{\partial T_l}, \tag{4}$$

where F_k is the net upward flux through level k and T_l is the temperature on level l. The elements of the Jacobian are calculated by perturbing, in turn, the temperature on each model level and calculating the fluxes at all levels. We include the full scattering and absorption properties of the

atmosphere in this calculation and calculate both solar fluxes and atmospheric IR fluxes for each perturbation. We also calculate the base-state fluxes B with no perturbation. Once J is calculated we then calculate the temperature changes δT required to cancel the residual fluxes to obtain a balanced solution. The residual fluxes are $-B$, such that the change will alter the base state flux B enough to cancel the net fluxes through all levels; that is,

$$J \cdot \delta T = -B. \tag{5}$$

The calculation is performed using a QR decomposition (Press et al. 1992) and the solution is exact for a square Jacobian, and minimizes the squared errors for nonsquare Jacobians. The same solution can also be obtained using an LU decomposition (Press et al. 1992), suggesting the numerical inversion is stable for the domain tested. Equation (4) is a linearized approximation to the full-sensitivity Jacobian, which would include nonlinear dependencies through the Planck function and absorption coefficients. In practice, the calculation is iterated until the δTs are small (e.g., <1 K for the radiative equilibrium calculation).

Where the vertical temperature gradient of the atmosphere is superadiabatic, the atmosphere should become unstable to convective overturning and the temperature profile should be pushed toward a convectively stable profile [e.g., the dry adiabat, Andrews et al. (1987)]. To calculate the radiative–convective equilibrium temperature (R/CET) profile, we first calculate the radiative equilibrium temperature (RET) profile as above and then stabilize the profile to convection by mixing potential temperature. We iterate this procedure with the RET calculation to ensure that both convective and radiative stability criteria are satisfied. In calculating the adiabatic lapse rate used to identify the convectively unstable regions we calculate the gravitational acceleration as described in Eq. (2) and the constant pressure heat capacity as described in Crisp (1986).

RESULTS

The RET and R/CET are calculated in four configurations. Vertical levels are prescribed using either the VIRA 81 vertical levels or the Lee et al. (2007) 32 vertical levels. For each vertical resolution, we allow the global mean solar fluxes to be internally calculated within the RTM [internally calculated solar flux (ICSF)] or prescribe the Tomasko et al. (1980) *nominal* solar flux model reproduced in Fig. 13 [fixed solar flux (FSF)]. The composition for each model is the same, as shown in Figs. 2 and 3, and the initial temperature profile is either the VIRA 0°–30° temperature profile (81 levels, Fig. 2) or the Lee et al. (2007) mean profile (32 levels, Fig. 11).

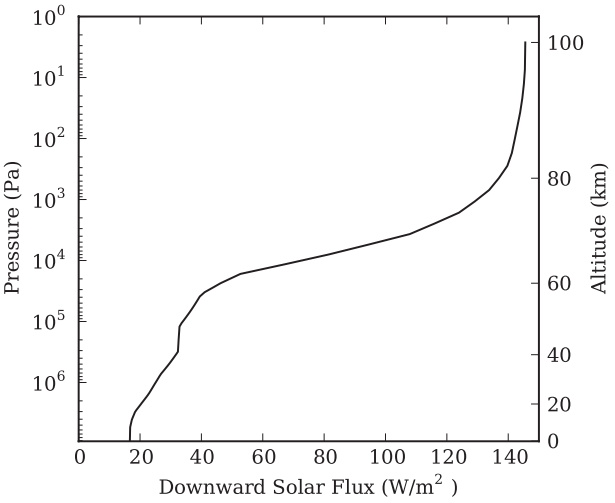

FIG. 13. Nominal solar flux profile calculated by Tomasko et al. (1980).

Figure 14 shows the RET profiles for the four experiments and the reference VIRA temperature profile for 0°–30° and 75°. All four experiments reproduce fairly well the same structure, with a small vertical temperature gradient above the cloud decks (below 10 kPa) and a large temperature gradient below the cloud decks. The ICSF and FSF models produce different equilibrated fluxes, which changes the middle atmosphere (100 kPa–100 Pa) structure, but there is very little difference in the lower atmosphere. The surface temperature in the four experiments is 850 ± 0.5 K (FSF) and 838 ± 4 K (ICSF) (the error bars give the difference between the two vertical resolutions). All four models have a temperature of 160–190 K at the model top with the ICSF model being slightly cooler. The (convectively stabilized) VIRA profiles have a surface temperature of 735 K and upper atmosphere temperature of ~175 K.

The greatest effect of the resolution change occurs in the cloud decks where the temperature and fluxes change most rapidly. In this region the increased resolution afforded by the 81-level model allows the profile to produce more extreme temperature gradients.

All four radiative equilibrium profiles are convectively unstable, particularly in the clouds at 100 kPa and near the surface. Figure 15 shows the same experiments when convection is included, with a surface temperature of 772 K (±2 K for the FSF models) or 757 K (±2 K for the ICSF models). Surface temperatures in both experiments have dropped because the upper atmosphere structure is tightly constrained by the incoming solar fluxes, and the lower atmosphere is, in turn, constrained by the upper atmosphere through the interactions within the opaque clouds and through convection.

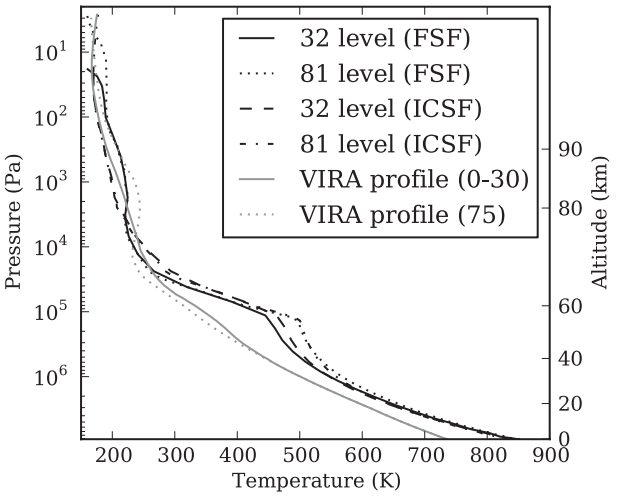

FIG. 14. Radiative equilibrium temperature profiles calculated for the composition given in Figs. 2 and 3. The calculation used either 32 levels defined in Lee et al. (2007) or the 81 vertical levels defined in Kliore et al. (1985). In the ICSF case the solar fluxes are calculated within the RTM. In the FSF case the solar fluxes are prescribed as given in Tomasko et al. (1980). Shown are the 32-level ICSF experiment (solid black), 32-level fixed solar flux experiment (dashed black), 81-level ICSF experiment (dotted black), 81-level fixed solar flux experiment (dashed–dotted black), and VIRA temperature profiles for 0°–30° (solid gray) and 75° (dashed gray) latitudes.

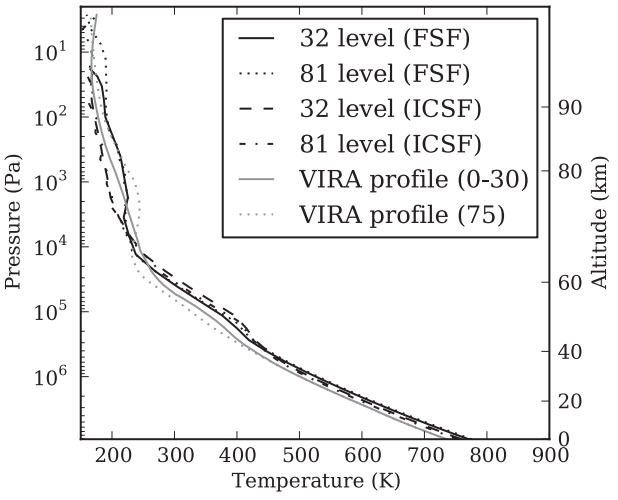

FIG. 15. Radiative–convective equilibrium temperature profiles calculated for the same conditions as the RET profiles/details as in Fig. 14.

All four experiments are now closer to the VIRA profile in the lower atmosphere. The ICSF models are closer to the lower atmosphere temperature profile of the VIRA profiles. The FSF models capture the location of the temperature maximum at 1 kPa better than the ICSF models. This may be because the cloud top used here is different to the cloud model assumed by Tomasko et al. (1980) (used in the calculation of solar fluxes in the FSF models).

The differences between the RET profiles (Fig. 14) and the R/CET profiles (Fig. 15) are not limited to the superadiabatic regions in the RET profile. The convective correction applied to the RET profile forces changes at all levels to maintain a radiative equilibrium (Fig. 16). This interaction is the cause for the decrease in the surface temperature, even though the lower atmosphere is slightly subadiabatic in the RET profile.

Net fluxes for the RET and R/CET profiles are shown in Figs. 17 and 18. In the RET models, the different outgoing TOA fluxes are caused by temperature variation at ~10 kPa (60 km), not in the tenuous upper atmosphere. The upper atmosphere (~1 kPa) contributes very little to the net TOA fluxes in these experiments, as indicated by the small flux gradient at pressures below that level. Additionally, in the RET models (Fig. 17) the surface fluxes are the same in all four models (16 W m^{-2}), whereas the TOA fluxes are 10% lower in the ICSF models compared to in the FSF models (145 W m^{-2} compared to 160 W m^{-2}). In radiative–convective equilibrium the net fluxes in the four experiments are significantly closer, with a TOA radiance of ~145 ± 2 W m^{-2}.

Figure 19 shows the spectral distribution of TOA net solar and IR radiation for the 81-level ICSF experiment at radiative equilibrium. Of the 160 W m^{-2} in the net *solar* insolation, 99% exists between 0.2 and 4.7 μm, and the median wavelength is 0.97 μm. In the net outgoing IR radiation, 99% exists between 5.1 and 38 μm, and the

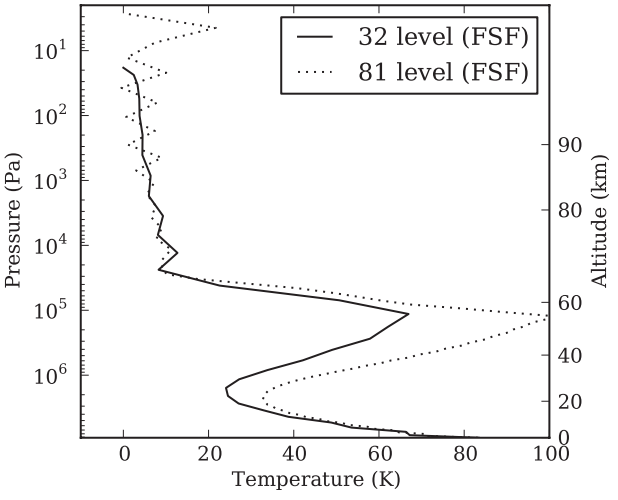

FIG. 16. Temperature difference between the RET (Fig. 14) and R/CET (Fig. 15) profiles (positive for RET > R/CET). In all cases, the convective adjustment stabilizes the profile by cooling the surface layers and cloud-bottom (40–50 km) layers.

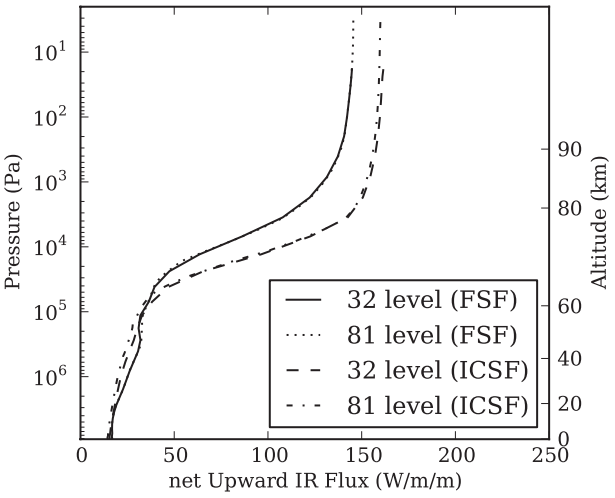

FIG. 17. Radiative equilibrium fluxes calculated for the composition given in Figs. 2 and 3; details as in Fig. 14, but no VIRA profiles plotted.

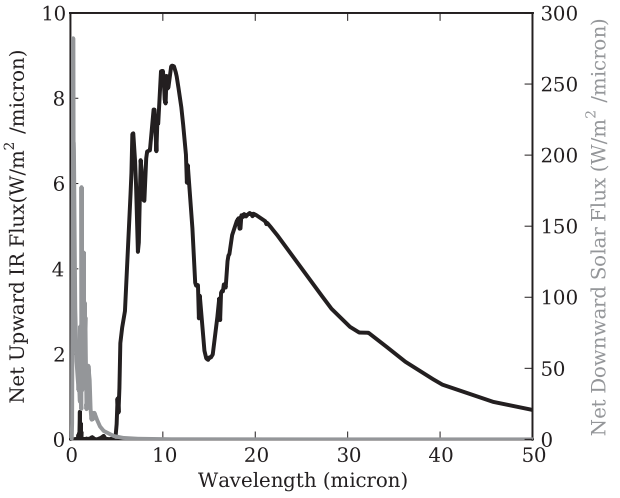

FIG. 19. TOA net fluxes for the 81-level ICSF RET profile: solar flux (black) and IR flux (gray).

median wavelength is 12.5 μm. This distribution suggests that we can terminate both IR and visible calculations at 5 μm, with IR (atmospheric fluxes) calculated above this value and solar fluxes calculated below.

Finally, the lapse rates for the convectively stabilized profiles (R/CET) are shown in Fig. 20 and agree well with the VIRA profiles, also shown. The simulated atmospheres are unstable near the surface and at 100 kPa (50–60 km). Above this unstable cloud region, there is a rapid change in the lapse rate to near 0 K km^{-1} (i.e., 10 K km^{-1} above the adiabat). All four experiments reproduce this structure with some variation.

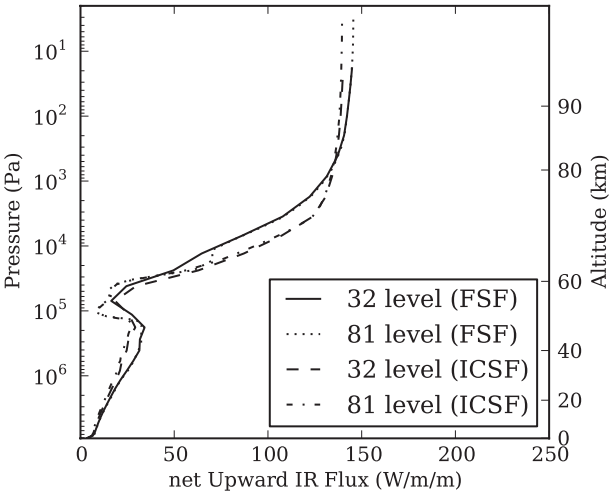

FIG. 18. Radiative–convective equilibrium fluxes calculated for the same conditions as the RET profiles given in Fig. 14; details as in Figs. 17 and 14.

c. Discussion

We have used our radiative transfer model to calculate radiative equilibrium temperature and radiative–convective equilibrium temperature profiles given the VIRA composition. In the four configurations that were tested, the RET profiles were unstable to convection and produced warmer than observed surface temperatures. When convection is included in the RTM, the adjustment lowered the surface temperature by almost 100 K and lowered the atmospheric thermal lapse rate

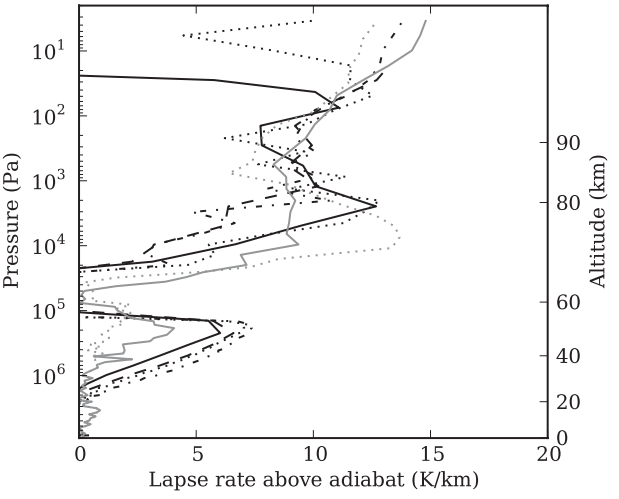

FIG. 20. Static stability for the R/CET profiles (K km^{-1}) given in Fig. 15, calculated as $\partial T/\partial z + g(z)/C_p(T)$, for the 32-level ICSF experiment (solid black), 32-level fixed solar flux experiment (dashed black), 81-level ICSF experiment (dotted black), 81-level fixed solar flux experiment (dashed–dotted black), and VIRA temperature profiles for 0°–30° (solid gray) and 75° (dashed gray) latitudes.

to more closely match the VIRA lower atmosphere temperature profile.

We compared the solar fluxes calculated by the RTM with fluxes prescribed by Tomasko et al. (1980), finding that our RTM calculated slightly higher net fluxes at radiative equilibrium but similar net fluxes at radiative–convective equilibrium, which is more representative of the observed atmosphere assumed by Tomasko et al.

5. Conclusions

We have developed a new radiative transfer model (RTM) suitable for use as a single-column model of the Venus atmosphere. This model includes the absorption and scattering effects of the most abundant absorbers and particulate cloud materials in the model, and also a number of the observationally derived continuum properties for those absorbers. We have shown that this model is able to reproduce both broad spectral features of the atmosphere of Venus and high-resolution spectra, given suitable inputs.

Using the VIRA temperature and composition profile, we derived visible albedo values and downward surface fluxes that agree well with those observed by orbiters (Drossart et al. 2007) and landers (Seiff et al. 1980; Avduevsky et al. 1983). We have also shown that we are able to replicate the radiance sensitivity within the near-IR ''windows'' that have been used to probe the surface and lower atmosphere of Venus (Tsang et al. 2008a; Mueller et al. 2008). Given a realistic temperature and composition profile the RTM is able to simulate the observations made by the VIRTIS instrument, at least in the relatively simple case of nighttime near-nadir emission.

We have used our RTM to investigate the solar heating and IR cooling used in a recent GCM and identified several errors in both the prescription of the radiation and in the specification of the heating function. We found that, when considered as a *radiative* heating profile, the parameterization given in Lee et al. (2007) provides too much radiative heating in the lower atmosphere compared with our RTM and that the relatively simple vertical profile of the prescribed heating does not capture the IR cooling at the bottom of the cloud decks. We suggest that the lower atmosphere convective adjustment may be better parameterized separately from the radiative forcing and that an additional IR cooling term be included in the parameterization.

Finally, we have used our RTM to derive radiative equilibrium temperature (RET) profiles and radiative–convective equilibrium temperature (R/CET) profiles and examined the ability of the model to produce an internally calculated solar flux profile by comparing the resulting temperature profiles with similar profiles calculated using a prescribed solar forcing (Tomasko et al. 1980). We found small differences between the internally calculated solar flux profile and the prescribed profile, which may be explained by differences in the assumed composition profiles and solar forcing of the models. We compared the temperature profiles resulting from these experiments with the VIRA temperature profile and found good agreement over the range of pressures investigated. Predicted surface temperatures were within 15 K for the R/CET profile using the internally calculated solar flux profile. Differences in the structure of the upper atmosphere can be attributed to differences in the composition and cloud altitudes in our model in comparison to the VIRA profiles and are not significant.

Acknowledgments. Numerical simulations in support of this research were performed on Caltech's Division of Geological & Planetary Sciences Dell cluster CITerra, and on the NASA Pleiades cluster. This work was performed under the NASA PATM Grant NNX07AF33G at the California Institute of Technology. We are grateful to Patrick Irwin for use of the Radtrans/NEMESIS code, Con Tsang and Colin Wilson for assistance with spectral data and the weighting function calculation, and Masahiro Takagi for advice on the carbon dioxide line shape in the Venus atmosphere. We thank the two anonymous reviewers for their insightful comments and suggestions that have helped improve this manuscript.

REFERENCES

Allen, D. A., and J. W. Crawford, 1984: Cloud structure on the dark side of Venus. *Nature,* **307,** 222–224.

Andrews, D. G., J. R. Holton, and C. B. Leovy, 1987: *Middle Atmosphere Dynamics*. Academic Press, 489 pp.

Avduevsky, V. S., M. Y. Marov, Y. N. Kulikov, V. P. Shari, A. Y. Gorbachevskiy, G. R. Uspenskiy, and Z. P. Cheremukhina, 1983: Structure and parameters of the Venus atmosphere according to Venera probe data. *Venus,* D. M. Hunten et al., Eds., The University of Arizona Press, 280–298.

Brion, C., M. Dyck, and G. Cooper, 2005: Absolute photoabsorption cross-sections (oscillator strengths) for valence and inner shell excitations in hydrogen chloride, hydrogen bromide and hydrogen iodide. *J. Electron Spectrosc. Relat. Phenom.,* **144,** 127–130.

Bullock, M., 1997: The stability of climate on Venus. Ph.D. thesis, University of Colorado, 254 pp.

——, and D. Grinspoon, 2001: The recent evolution of climate on Venus. *Icarus,* **150,** 19–37.

Chan, W., G. Cooper, R. Sodhi, and C. Brion, 1993: Absolute optical oscillator strengths for discrete and continuum photoabsorption of molecular nitrogen (11–200 eV). *Chem. Phys.,* **170,** 81–97.

Clough, S. A., F. X. Kneizys, and R. W. Davies, 1989: Line shape and the water vapor continuum. *Atmos. Res.,* **23,** 229–241.

Colin, L., 1983: Basic facts about Venus. *Venus,* D. M. Hunten et al., Eds., The University of Arizona Press, 10–26.

Crisp, D., 1986: Radiative forcing of the Venus mesosphere. I. Solar fluxes and heating rates. *Icarus,* **67,** 484–514.

——, 1989: Radiative forcing of the Venus mesosphere. II. Thermal fluxes, cooling rates, and radiative equilibrium temperatures. *Icarus,* **77,** 391–413.

Drossart, P., and Coauthors, 2007: Scientific goals for the observation of Venus by VIRTIS on ESA/Venus Express mission. *Planet. Space Sci.,* **55,** 1653–1672.

Esposito, L. W., J.-L. Bertaux, V. Krasnoplosky, V. I. Moroz, and L. V. Zasova, 1997: Chemistry of lower atmosphere and clouds. *Venus II,* S. W. Bougher, D. M. Hunten, and R. S. Phillips, Eds., The University of Arizona Press, 415–458.

Eymet, V., R. Fournier, S. Blanco, and J. Dufresne, 2005: A boundary-based net-exchange Monte Carlo method for absorbing and scattering thick media. *J. Quant. Spectrosc. Radiat. Transfer,* **91,** 27–46.

Feng, R., G. Cooper, and C. Brion, 1999: Absolute oscillator strengths for hydrogen sulphide: I. Photoabsorption in the valence-shell and the S 2p and 2s inner-shell regions (4–260 eV). *Chem. Phys.,* **244,** 127–142.

Goody, R., and Y. Yung, 1995: *Atmospheric Radiation: Theoretical Basis*. Oxford University Press, 519 pp.

Gropp, W., E. Lusk, and A. Skjellum, 1999: *Using MPI: Portable Parallel Programming with the Message Passing Interface*. The MIT Press, 371 pp.

Hollingsworth, J., R. Young, G. Schubert, C. Covey, and A. Grossman, 2007: A simple-physics global circulation model for Venus: Sensitivity assessments of atmospheric superrotation. *Geophys. Res. Lett.,* **34,** L05202, doi:10.1029/2006GL028567.

Ingersoll, A., 1969: The runaway greenhouse: A history of water on Venus. *J. Atmos. Sci.,* **26,** 1191–1198.

Irwin, P., S. Calcutt, and F. Taylor, 1997: Radiative transfer models for Galileo NIMS studies of the atmosphere of Jupiter. *Adv. Space Res.,* **19,** 1149–1158.

——, and Coauthors, 2008: The NEMESIS planetary atmosphere radiative transfer and retrieval tool. *J. Quant. Spectrosc. Radiat. Transfer,* **109,** 1136–1150.

Johns, T., R. Carnell, J. Crossley, J. Gregory, J. Mitchell, C. Senior, S. Tett, and R. Wood, 1997: The second Hadley Centre coupled ocean–atmosphere GCM: Model description, spinup and validation. *Climate Dyn.,* **13,** 103–134.

Kliore, A., V. Moroz, and G. Keating, Eds., 1985: The Venus International Reference Atmosphere. *Adv. Space Res.,* **5** (11), 1–305.

Knollenberg, R., and D. Hunten, 1980: The microphysics of the clouds of Venus—Results of the Pioneer Venus particle size spectrometer experiment. *J. Geophys. Res.,* **85,** 8039–8058.

Kylling, A., K. Stamnes, and S. Tsay, 1995: A reliable and efficient two-stream algorithm for spherical radiative transfer: Documentation of accuracy in realistic layered media. *J. Atmos. Chem.,* **21,** 115–150.

Lacis, A., and V. Oinas, 1989: A description of the correlated *k* distribution method for modeling nongray gaseous absorption, thermal emission, and multiple scattering in vertically inhomogeneous atmospheres. *J. Geophys. Res.,* **96** (D5), 9027–9063.

Lebonnois, S., F. Hourdin, V. Eymet, A. Crespin, R. Fournier, and F. Forget, 2010: Superrotation of Venus' atmosphere analyzed with a full general circulation model. *J. Geophys. Res.,* **115,** E06006, doi:10.1029/2009JE003458.

Lee, C., S. R. Lewis, and P. L. Read, 2007: Superrotation in a Venus general circulation model. *J. Geophys. Res.,* **112,** E04S11, doi:10.1029/2006JE002874.

Manatt, S., and A. Lane, 1993: A compilation of the absorption cross-sections of SO_2 from 106 to 403 nm. *J. Quant. Spectrosc. Radiat. Transfer,* **50,** 267–276.

Meadows, V. S., and D. Crisp, 1996: Ground-based near-infrared observations of the Venus nightside: The thermal structure and water abundance near the surface. *J. Geophys. Res.,* **101,** 4595–4622.

Molina, L., J. Lamb, and M. Molina, 1981: Temperature dependent UV absorption cross sections for carbonyl sulfide. *Geophys. Res. Lett.,* **8,** 1008–1011.

Moroz, V., 1983: Stellar magnitude and albedo data of Venus. *Venus,* D. M. Hunten et al., Eds., The University of Arizona Press, 27–35.

——, A. Ekonomov, B. Moshkin, H. Revercomb, L. Sromovsky, and J. Schofield, 1985: Solar and thermal radiation in the Venus atmosphere. *Adv. Space Res.,* **5,** 197–232.

Moskalenko, N., I. Ilin, S. Parzhin, and L. Rodionov, 1979: Pressure-induced infrared radiation absorption in atmospheres. *Akad. Nauk SSSR,* **15,** 912–919.

Mueller, N., J. Helbert, G. L. Hashimoto, C. C. C. Tsang, S. Erard, G. Piccioni, and P. Drossart, 2008: Venus surface thermal emission at 1 μm in VIRTIS imaging observations: Evidence for variation of crust and mantle differentiation conditions. *J. Geophys. Res.,* **113,** E00B17, doi:10.1029/2008JE003118.

Palmer, K., and D. Williams, 1975: Optical constants of sulfuric acid; application to the clouds of Venus? *Appl. Opt.,* **14,** 208–219.

Pollack, J. B., and R. E. Young, 1975: Calculations of the radiative and dynamical state of the Venus atmosphere. *J. Atmos. Sci.,* **32,** 1025–1037.

Press, W., S. Teukolsky, W. Vetterling, and B. Flannery, 1992: *Numerical Recipes in C*. Cambridge University Press, 994 pp.

Rodgers, C., 2000: *Inverse Methods for Atmospheric Sounding: Theory and Practice*. World Scientific, 238 pp.

Rothman, L., R. B. Wattson, R. Gamache, J. W. Schroeder, and A. McCann, 1995: HITRAN HAWKS and HITEMP: High temperature molecular database. *Atmospheric Propagation and Remote Sensing IV,* J. C. Dainty, Ed., International Society for Optical Engineering (SPIE Proceedings, Vol. 2471), 105–111.

——, and Coauthors, 2005: The HITRAN 2004 molecular spectroscopic database. *J. Quant. Spectrosc. Radiat. Transfer,* **96,** 139–204.

Seiff, A., 1983: Thermal structure of the atmosphere of Venus. *Venus,* D. M. Hunten et al., Eds., The University of Arizona Press, 215–279.

——, D. B. Kirk, R. E. Young, R. C. Blanchard, J. T. Findlay, G. M. Kelly, and S. C. Sommer, 1980: Measurements of thermal structure and thermal contrasts in the atmosphere of Venus and related dynamics observations: Results from the four Pioneer Venus probes. *J. Geophys. Res.,* **85,** 7903–7933.

Stamnes, K., S. Tsay, W. Wiscombe, and I. Laszlo, cited 2000: DISORT, a general-purpose Fortran program for discrete ordinate-method radiative transfer in scattering and emitting layered media: Documentation of methodology. [Available online at ftp://climatel.gsfc.nasa.gov/wiscombe.]

Taylor, F. W., and Coauthors, 1980: Structure and meteorology of the middle atmosphere of Venus: Infrared remote sensing from the Pioneer Orbiter. *J. Geophys. Res.,* **85,** 7963–8006.

Titov, D., M. Bullock, D. Crisp, N. Renno, F. Taylor, and L. Zasova, 2007: Radiation in the atmosphere of Venus. *Exploring Venus as a Terrestrial Planet, Geophys. Monogr.,* Vol. 176, Amer. Geophys. Union, 121–138.

Tomasko, M., and Coauthors, 1980: The thermal balance of Venus in light of the Pioneer Venus Mission. *J. Geophys. Res.,* **85** (A13), 8187–8199.

Tsang, C. C. C., P. G. J. Irwin, F. W. Taylor, and C. F. Wilson, 2008a: A correlated-*k* model of radiative transfer in the near-infrared windows of Venus. *J. Quant. Spectrosc. Radiat. Transfer,* **109,** 1118–1135.

——, and Coauthors, 2008b: Tropospheric carbon monoxide concentrations and variability on Venus from Venus Express/VIRTIS-M observations. *J. Geophys. Res.,* **113,** E00B08, doi:10.1029/2008JE003089.

Washburn, E., and C. West, 1926: *International Critical Tables of Numerical Data, Physics, Chemistry and Technology*. National Research Council, 344 pp.

Weisstein, E. W., cited 2003: Gaussian quadrature. [Available online at http://mathworld.wolfram.com/GaussianQuadrature.html.]

Yamamoto, M., and M. Takahashi, 2003: The fully developed superrotation simulated by a general circulation model of a Venus-like atmosphere. *J. Atmos. Sci.,* **60,** 561–574.

——, and ——, 2006: Superrotation maintained by meridional circulation and waves in a Venus-like AGCM. *J. Atmos. Sci.,* **63,** 3296–3314.